



Research Article

Self-assembling nacre-like high-strength and extremely tough polymer composites with new toughening mechanism



Yu Bu^{a,b,1}, Xu Wang^{c,1}, Xiuming Bu^d, Zhengyi Mao^e, Zhou Chen^e, Zebiao Li^{a,b}, Fengqian Hao^{a,b}, Johnny C. Ho^d, Jian Lu^{a,b,e,*}

^a CityU-Shenzhen Futian Research Institute, Shenzhen 518045, China

^b Centre for Advanced Structural Materials, City University of Hong Kong Shenzhen Research Institute, Greater Bay Joint Division, Shenyang National Laboratory for Materials Science, 8 Yuexing 1st Road, Shenzhen Hi-Tech Industrial Park, Nanshan District, Shenzhen 518000, China

^c MOE Key Laboratory of Impact and Safety Engineering, Ningbo University, Ningbo 315211, China

^d Department of Materials Science and Engineering, City University of Hong Kong, Hong Kong SAR 999077, China

^e Department of Mechanical Engineering, City University of Hong Kong, Hong Kong SAR 999077, China

ARTICLE INFO

Article history:

Received 15 April 2022

Revised 24 May 2022

Accepted 30 May 2022

Available online 18 August 2022

Keywords:

Polymer composites

Metallic glass thin film

Toughness

Toughening mechanism

Nacre-like fracture

ABSTRACT

Achieving high strength, deformability and toughness in polymers is important for practical industrial applications. This has remained challenging because of the mutually opposing effects of improvements to each of these properties. Here, a self-assembling nacre-like polymer composite is designed to achieve extremely tough with increasing strength. This special design significantly improved polymer's mechanical properties, including an ultra-high fracture strain of 1180%, a tensile strength of 55.4 MPa and a toughness of 506.9 MJ/m³, which far exceed the highest values previously reported for polymer composites. This excellent combination of properties can be attributed to a novel toughening mechanism, achieved by the synergy of the domain-limiting effect of metallic glass fragments with the strain-gradient-induced orientation and crystallisation within the polymer during stretching. Our approach opens a promising avenue for designing robust polymer materials in armour and aerospace engineering for a range of innovative applications.

© 2022 Published by Elsevier Ltd on behalf of The editorial office of Journal of Materials Science & Technology.

1. Introduction

Soft materials are becoming increasingly important in many fields, especially in the development of several new and high-tech industries, such as the manufacture of aircraft tires, optical lenses and surgical implants, fuelling a long-term demand for the production of polymers that combine high strength and toughness with other specific physical properties [1,2]. Extensive efforts have been made to strengthen and toughen polymers over the past few years, and many significant advances have been made [3–5]. Normally, the traditional modification method can be divided into two types, mainly including molecular chains composition/structure design and foreign implants introduction. For the former, although the strength of the material is increased, the improvement in toughness is limited, which may be due to the suppressive dissipation effect of the rheological behaviour as the sliding and decoupling

of the chains are replaced by strong covalent bonds [6–12]. For the latter, theoretically, the mechanical properties of a composite material will lie in a range limited by their components, thus the addition of implants also decreases the composite's toughness owing to their low deformability, which has been noted with particle-reinforced polymers [13–17] and fibre-reinforced materials [18–24].

The design of laminated structure, introducing a metal layer on the polymer surface, has been investigated as a possible strategy to affect the mechanical properties of polymer [25–29]. Xiang et al. had reported a strain localization phenomenon in the deformation process of a reinforced polymer with metal film [27], and studied the influence of a copper film thickness on the fracture limit of metallic part of a film composite [25]. However, such research has mainly focused on the conductivity of metal films and neglected to thoroughly investigate the overall mechanical properties of metal/polymer film composites. In 2009, Gupta et al. used pure Al film and polyethylene terephthalate (PET) to prepare thin-film composite materials by vacuum thermal deposition, which achieved toughening from 25% to 81% while reducing strength from 108.88 MPa to 99.25 MPa [30].

* Corresponding author at: CityU-Shenzhen Futian Research Institute, Shenzhen 518045, China.

E-mail address: jianlu@cityu.edu.hk (J. Lu).

¹ These authors contributed equally to this work.

In this work, a self-assembling biomimetic material with an initial laminated structure is designed. Unlike the traditional designs, the polymer film composites studied herein demonstrate toughness limits beyond those predicted by continuum mechanics, in addition to the generally understood strengthening effect of compositing. This approach constructs a complex deformation field to make the rheological process nonaffine during deformation, which creates a more oriented state with higher fracture resistance, with the strain induced crystallisation further improving the polymer's strength and toughness. Meanwhile, the strengthening and toughening effect of this composite is combined with a self-assembling nacre-like behaviour. Systematic experimental characterisation and finite element method (FEM) analysis reveal the mechanism of this new toughening phenomenon. These composites can be stretched almost 12 times their initial length and exhibit both high tensile strength and high toughness of 52 MPa and 506.9 MJ/m³, respectively, via this new toughening mechanism.

2. Experimental

2.1. MgZnCa/PET composite films preparation

A commercially available PET film of dimensions 7 cm × 7 cm with a thickness of 200 μm was used as the substrate for MgZnCa film deposition. A commercially available Angstrom deposition system was used to produce amorphous MgZnCa thin films of various thicknesses on PET substrates by DC magnetron sputtering in Ar (purity > 99.99%). The PET substrates had been cleaned by acetone, alcohol and distilled water for 15 min separately. They were also cleaned by Ar ion sputtering to remove any surface contaminants. The deposition system included a vacuum chamber equipped with a rotatable sample stage and four circular planar magnetrons 6'' and 3'' in diameter. A turbo molecular pump with a rotary pump was used to evacuate the chamber. Substrates were located on the rotating stage, approximately 13 cm from the target substrate. The sample stage rotation was maintained at 15 rpm to provide a uniform film. The sputtering process was performed in Ar with a working pressure of 0.5 Pa and an external substrate bias of -50 V; the deposition rate was 11 nm min⁻¹, and the substrate temperature was maintained at room temperature.

2.2. Characterization methods

The uniaxial tensile tests used rectangle-shaped samples of 60 mm × 5 mm, cut from the amorphous PET and MZC/PET films. The tensile tests were performed on three specimens per sample, with a gauge length of 20 mm and a tensile rate of 15 mm min⁻¹ using a mechanical testing system (Tinius Olsen) at room temperature.

The morphological structures of the samples were analyzed by field-emission SEM (FEI Quanta 450) and AFM (Bruker Dimension Icon) in tapping mode. These samples were Au-sputtered before scanning. The morphological structure was analyzed in the view fields of 10 μm × 10 μm. The orientation and crystallisation of the original and stretched PET and MZC/PET films were investigated by an X-ray diffractometer (Bruker) with Cu Kα radiation (λ = 0.154 nm). The 2θ scan data were collected at 0.02° intervals over ranges of 5°–60°. FTIR (Shimadzu) was used to detect the absorption spectra in the frequency region 400–4000 cm⁻¹. The microstructures of the thin films were examined by transmission electron microscopy (TEM; JEOL 2100) at 200 kV. TEM samples were prepared with focused ion beam equipment. The thin films were examined by EDS to determine their precise atomic compositions.

2.3. Finite element simulation method of MZC/PET composites

To simulate the large deformation of the specimen, the non-linear geometry effects and hyperelastic-plasticity of the polymer are required. The MZC film was modelled by shell elements and the connection between the metal film and polymer matrix was considered to be perfectly bonded. The thicknesses of the polymer substrate and metal film were considered equal in the experiment, with 'dog bone' shaped ends built into the model to make the deformation uniform within the region of the gauge length. The shape and size of the film fragments and the space between them were examined in SEM images of the sample, showing that their distribution was random. For the bonding between the metal fragments and the polymer, a Lagrangian mesh was adopted instead of a Eulerian mesh because of the latter's disadvantage in simulating deformation continuity between solid and liquid-like parts. Thus, the displacement boundary conditions acting on the two end surfaces of the model were designed to make the calculation stable. In the simulation, the gauge length of the model was 1 mm and the total length was 2.4 mm. The mechanical properties of the polymer were derived from the experimental data, with the metal film simulated as a brittle surface with a Young's modulus 1.73 GPa, which was calculated from the stress-strain characteristics of the PET and MZC/PET. The displacement of the two end faces was controlled in opposite directions along the tensile axis, making the average strain rate in the investigated region the same as in the tensile experiment.

3. Results and discussion

3.1. Material design

In polymer, the entropic elasticity and dissipation associated with the uncoupling of the junctions (crosslinks or entanglement points in the network) are the two dominating mechanisms of deformation [31]. However, the microstructure of the molecular chain network does not correspond directly to the strain during nonaffine deformation. Numerous studies have shown that the introduction of stress can orient molecular chains, which increases the strength because the energy required to break covalent bonds is much larger than that of van der Waals and hydrogen bonds [32,33]. This phenomenon implies the possibility of a new strengthening and toughening mechanism, whereby strength and toughness will both be improved if the microstructure of the polymer is reconstructed in a more oriented way at the same strain. Relevant investigations have proven that stress is a driving force for the junction flow, but in most cases the deformation of the material is homogeneous, resulting in an affine deformation of the molecular chain network [32,34]. Therefore, a new toughening mechanism can be envisioned in which the nonaffine flow of junctions or entanglement points is achieved by constructing complex strain fields in PET substrate to obtain a more oriented microstructure to resist stronger loads and achieve higher strength and toughness.

Nacre-like biomaterials with unrivalled mechanical robustness have been investigated in recent decades [35–37]. Their unexpected toughness is attributed to their complex multi-layer hierarchical structure, where the relative sliding between the brittle aragonite platelets dissipates energy while the monolayers act as strong fracture deflectors and terminators [38–40]. The complex structure of nacre inspires the construction of the required strain field, while its toughening mechanism also works in conjunction with the 'orientation' mechanism to improve the overall performance of the material [39,40]. The design of nacre-like biomaterials typically requires precise dimensional control of the microstructure because of the complicated deformation mechanism,

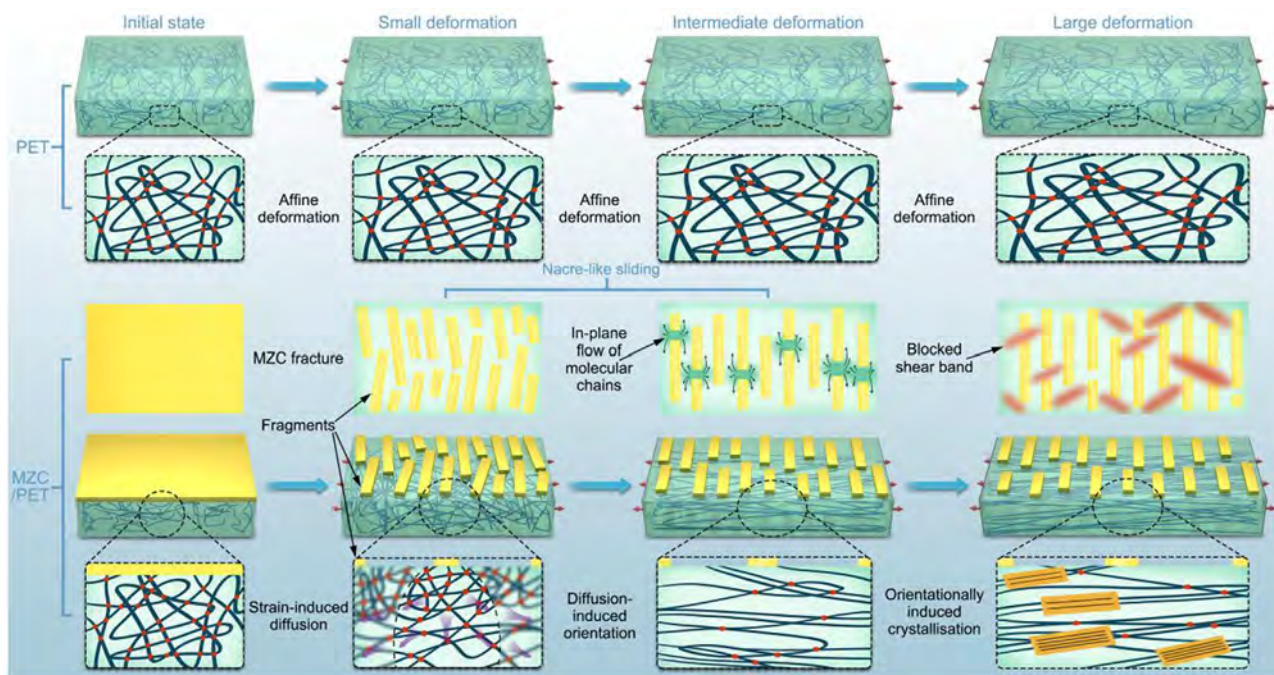


Fig. 1. Schematic illustration of the design of polymer composites.

which leads to high fabrication cost [36,40]. By contrast, the new approach here simply utilizes the hierarchical structure itself, while the toughening effect of the nacre only plays an auxiliary role. Thus, there are no strict requirements for the dimensions of the microstructure, which can be formed via self-assembly to reduce costs.

The design of the composite is shown in Fig. 1: a strong, thin, brittle coated $\text{Mg}_{60}\text{Zn}_{35}\text{Ca}_5$ (MZC) metal film lying on a thick polyethylene terephthalate (PET) substrate. When the MZC/PET composite is loaded, the low toughness of the MZC metallic film makes it break into fragments of a size determined by the interfacial topography firstly. As the deformation continues, the tightly adhered MZC fragments severely limit the deformation of the top surface of the polymer, while the bottom surface remains free because of its sufficient thickness, making the deformation here uniform. The marked difference in deformation behaviour between the limited top surface and unlimited bottom one generates a huge strain gradient with corresponding stresses, which accelerate and drive the junctions to flow to the low-free-energy oriented state, as shown in Fig. 1. Thus, the nacre-like structure, the nonaffine deformation and the orientation of the chains are achieved via self-assembly without any external operation, improving the material's strength and toughness.

3.2. Preparation and materials characterization

To achieve the approach presented in Fig. 1, the polymeric substrate must have perfect fluidity so that it will be oriented under the load at room temperature. According to previous studies, PET shows a high degree of orientation under tension [32], so it was selected to be the substrate of the composite. Furthermore, the coating film must be sufficiently brittle to form the desired fragments and strong enough to limit the deformation of the polymer without peeling, making metallic glass a suitable choice. With these considerations, a series of laminated composites with an MZC metallic film coated on a PET substrate were designed. MZC films with different thicknesses (0.3, 1 and 1.5 μm) were deposited using magnetron sputtering (as shown in Fig. S1(a)) onto commer-

cial PET with a thickness of 200 μm . Single and double-sided coatings were prepared on the 0.3 μm and 1 μm substrates, while only single-sided coatings were prepared for the 1.5 μm MZC. Before the film formation, the PET surface was cleaned and modified by Ar plasma to improve its surface activity and surface energy, and make it more binding with the MZC film. We tested the surface energy of the PET material before and after modification. From the comparison of the contact angle of water droplets at the interface, shown in Fig. S2, it can be clearly seen that the contact angle of the PET surface decreases significantly after plasma activation, indicating that its surface energy increases, and the adsorption tendency of the PET interface to the MZC film also increases, so it has good adhesion to the MZC thin film, which can be seen from the high-resolution TEM image, shown in Fig. S1(b). The perfect matching of the MZC/PET interface shown in transmission electron microscopy implies that there was good adhesion between the two layers, which will also limit the degradation of properties caused by any fabrication defects. In addition, the fast Fourier transform graph (inset of Fig. S1(c)) also shows an amorphous ring corresponding to the MZC structure, which presents the same elastic-brittle mechanical properties as normal metallic glass. To characterise the chemical composition and physical bonding states of the PET, stretched PET and MZC/PET composites (polymer side and metal side), Fourier transform infrared spectroscopy (FTIR) was carried out, as shown in Fig. S3. The FTIR results show six major absorption bands, which are attributed as follows: (1) 1710 cm^{-1} is the stretching of $-\text{C}=\text{O}$ present in ester groups; (2) 1409 cm^{-1} is the characteristic band of disubstituted benzene rings; (3) 1243 cm^{-1} and (4) 1092 cm^{-1} are the asymmetric stretching of $-\text{C}-\text{C}-\text{O}$ and $\text{O}-\text{C}-\text{C}$, respectively; and (5) 1012 cm^{-1} and (6) 720 cm^{-1} arise from the benzene ring and the C-H vibrations of aromatic structures, respectively [41]. The peak widths and positions of the absorption bands of stretched PET and stretched MZC/PET coincide with those of the unstretched films. This indicates that the major chemical groups of the PET-based samples were uniform and that the molecular structure was not changed significantly by the MZC deposition. Furthermore, the elemental composition of the MZC/PET composite film was deter-

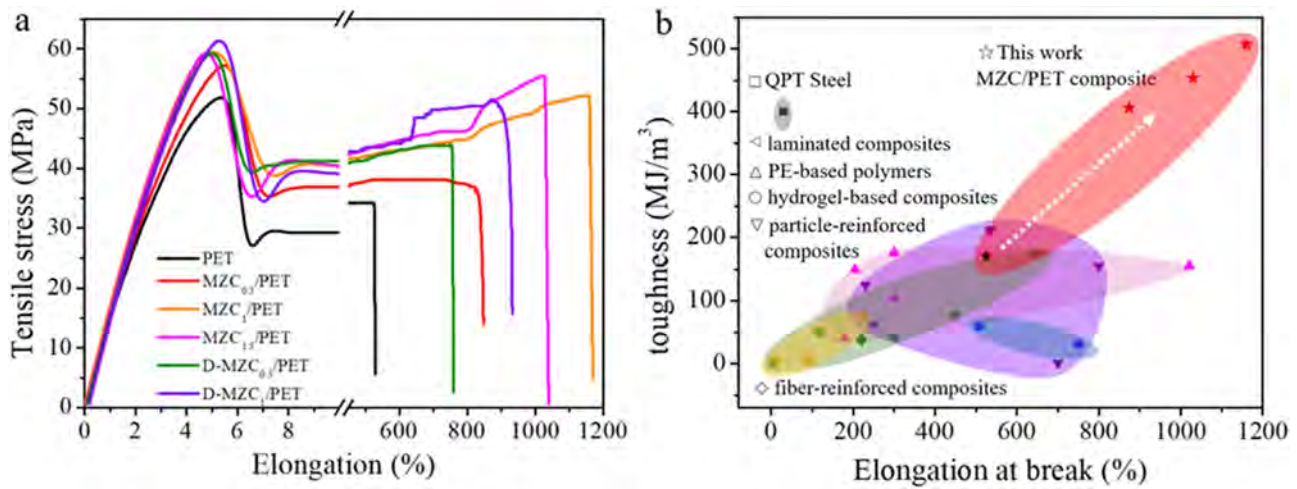


Fig. 2. (a) Stress-strain curves of PET and MZC/PET composites. (b) Dependence of toughness on elongation at break of different materials: hydrogel-based composites [8,42], polyethylene (PE) based polymers [6,10–12, 43], particle-reinforced polymer composites [13–17], fibre-reinforced composites [18–23] and laminated composites [30,39,44], quenching-partitioning-tempering (QPT) steel [49].

mined by scanning electron microscopy (SEM) and energy dispersive X-ray spectroscopy (EDS) of samples subjected to 300% tensile strain, as shown in Fig. S4. The distribution of various elements and fragments at the boundary is observed clearly in the mapping diagram. Table S1 summarises the element composition corresponding to the coating layer fragments (Spectrum 2) and the tertiary cracks (Spectrum 1) scanned in Fig. S4(a). Here, spectrum 1 is the polymer composed of C and O and Spectrum 2 is composed of Mg, Zn and Ca, which is the as-deposited $Mg_{60}Zn_{35}Ca_5$ amorphous film with the same nominal composition as the sputtering target.

3.3. Mechanical properties of MZC/PET composite

The mechanical properties of PET and MZC/PET composites were investigated by uniaxial tensile testing at the quasi-static condition with a strain rate of $1.25 \times 10^{-3} \text{ s}^{-1}$. Fig. 2(a) shows the stress-strain curves of the PET and MZC_x/PET (x : 0.3 μm , 1 μm , 1.5 μm) and double-side coated MZC/PET ($D-MZC_x/PET$, x : 0.3 μm , 1 μm) composites. The single-side coated MZC_1/PET exhibited surprisingly highest tensile strains of 1180%, which is higher than that of $MZC_{0.3}/PET$ (845%) and MZC_1/PET (1030%), respectively (the digital photo of the stretched MZC_1/PET was shown in Fig. S5(b)). This superior deformation capacity is almost twice that of PET (525%) and far exceeds that of MZC metallic glass film (less than 2%), even though those materials are the principal components. In the general theory of composite mechanics, a mismatch between the mechanical properties of the components leads to a deformation concentration, which first destroys the weaker component, leaving the stronger component to bear the full load acting on the composite alone, so that the effective properties of the composite lie between them of the components. By contrast, this rule is clearly broken for the MZC/PET composites, with the induced brittle MZC film toughening the PET substrate far beyond either of their original ultimate elongations. Fig. 2(a) displays that this toughening effect tends to increase when the thickness of the MZC film is small, with the ultimate toughness value reached at a critical thickness, combined with an expected increase in strength. And a thicker MZC film the stronger fragments and limitation effects, which will cause a greater strain gradient in the thickness direction, and so the orientation of the molecular chains. Thus within a certain range, the increase in the thickness of the MZC film will present a positive effect on the strengthen and toughen of the

composite material. Moreover, the comparison between the single and double-sided coatings shows a conventional trade-off between the material's strength and toughness, where a larger proportion of metallic film brings higher strength but lower toughness. The strength and toughness of the double-sided MZC_1/PET composites are lower than those of the single-sided coated film with 1.5 μm thickness, indicating that this new strengthening and toughening mechanism is more effective for single-sided coatings.

The toughness of the samples is summarised in Table S2. Fig. 2(b) shows a comparison of the mechanical robustness, in terms of elongation at break and toughness, among various types of polymer composites, including hydrogel-based composites [8,42], polyethylene (PE) based polymers [6,10–12,43], particle-reinforced polymer composites [13–17], fibre-reinforced composites [18–23] and laminated composites [30,39,44]. As predicted by mechanical theory, laminated composites show a relatively low toughness and elongation because of the limitations of their weaker component. Similarly, fibre- and particle-reinforced composites exhibit higher strength because of their stronger inclusions, but their elongation is limited by the stress concentrations. Particle-reinforced composites show better mechanical properties, which are attributed to the more complex interactions between the inclusions and matrix, partially dissipating energy. Although polyethylene-based and hydrogel-based composites (such as poly(ethylene glycol)-based material [12] and dipole-dipole and hydrogen bonding-reinforced hydrogels [8]) exhibit considerable fracture strain, the molecular chain network characteristics and constituents confer a low strength, resulting in their low toughness. In contrast, the MZC_x/PET composite exhibits a high toughness of 506.9 MJ/m^3 (MZC_1/PET) and also a large fracture strain than those of the modified polymers, which implies a greater energy absorption capability. Additional features of the mechanical properties in the stress-strain curves are summarised in Table S2.

3.4. Nacre-like mechanical behavior

The stretching process of the MZC/PET composite at different elongations was captured by a high-definition camera, as shown in Fig. 3(a). From a macro-perspective, the 'break state' of the MZC film appears as a line crossing the sample perpendicular to the loading direction combined with initial necking, which is the stress localisation during the loading process. As the deformation continued, the breaking region evolved along the loading direction,

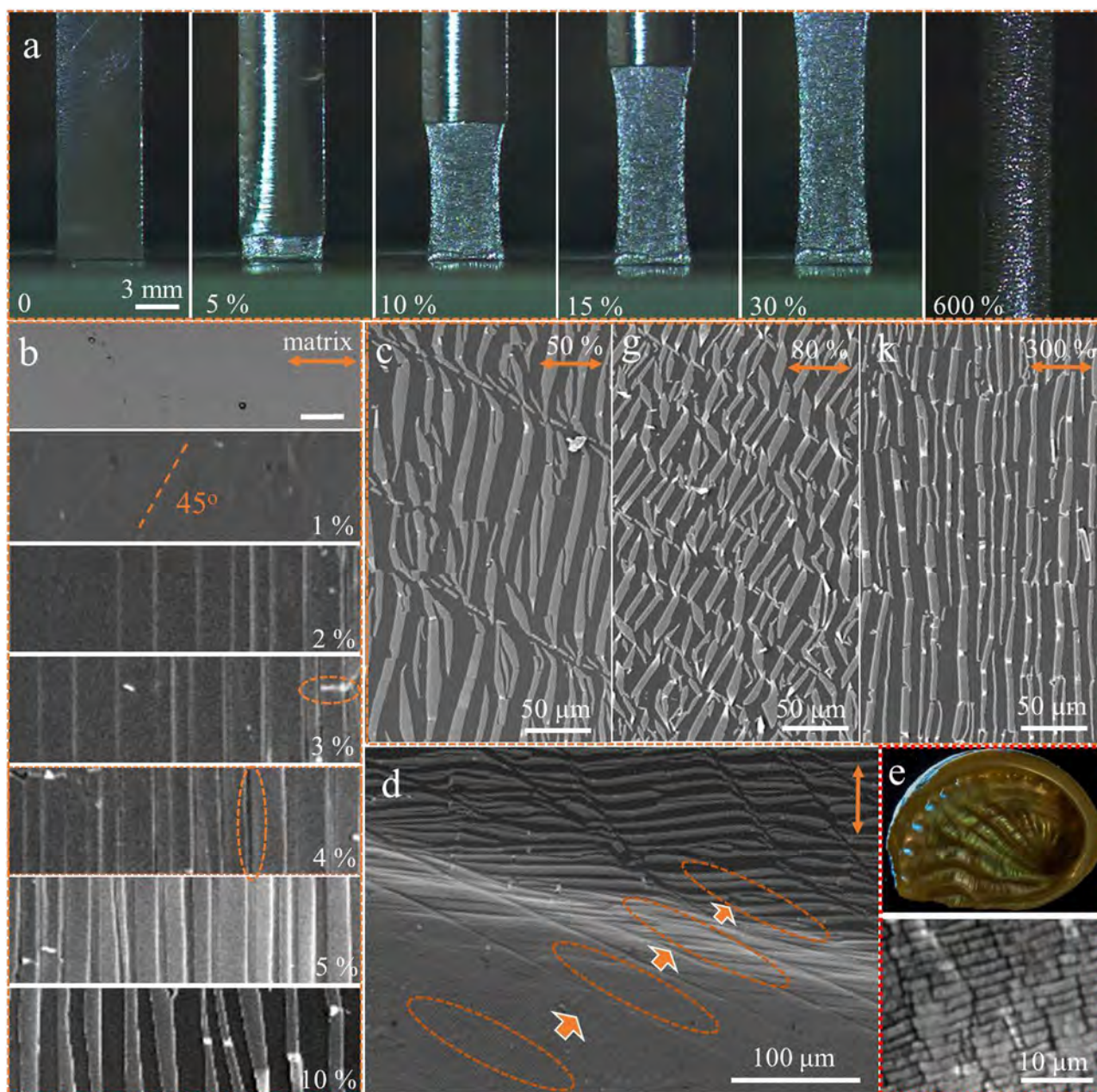


Fig. 3. (a) Photographs of the stretching process of the MZC/PET composite with different elongations. (b–d) SEM images of the fracture evolution in MZC/PET composite at different elongations. (e) Images of natural nacre (above) and the microstructure of nacre (below). Reproduced with permission [38], 2007, Elsevier. Ltd. The direction of the orange arrow in the upper right corner of the figure corresponds to the direction of stretching.

which is contrary to the deformation and instability rule that the localisation of the deformation relaxes with the growing stress. To further examine the crack development process, SEM was performed on stretched samples with different strains. Fig. 3(b) illustrates the fragmentation process of the MZC coating on the PET substrate during the test. A crack first appeared in the MZC film at an angle of 45° to the stretching direction at 1% strain, which corresponds to the direction of the maximum shear stress in brittle metallic glass film under uniform tension. The uniform cracks then rapidly developed approximately perpendicular to the stretching direction at 2% strain between the oblique cracks, with vertical cracking of the fragments subsequently initiated. These cracks developed along the tensile direction because of the lateral contraction of the sample resulting from the Poisson effect [45]. At approximately 4% strain, tertiary cracks appeared parallel to the pri-

mary cracks, breaking the metal pieces into smaller fragments. The fragments ranged from 1.5 μm to 3 μm in width and 15 μm to 40 μm in length, as determined by the surface topography of the PET, which was characterised by SEM and atomic force microscopy (AFM) as shown in Fig. S6(a) and (b), respectively.

After the primary cracks appeared at 45° to the stretching direction, the following formed cracks were almost perpendicular to the load direction within a tolerance of 20°. This resulted in the slanted fragments shown in the schematic diagram in Fig. 1 and the morphology at 50% strain shown in Fig. 3(c). During continuing tension, these fragments turned towards the direction perpendicular to the load. When the strain increased to 80%, the fragments exhibited a wavy shape and turned towards the horizontal direction. When the strain increased to 300%, the fragments became almost completely perpendicular to the load direction,

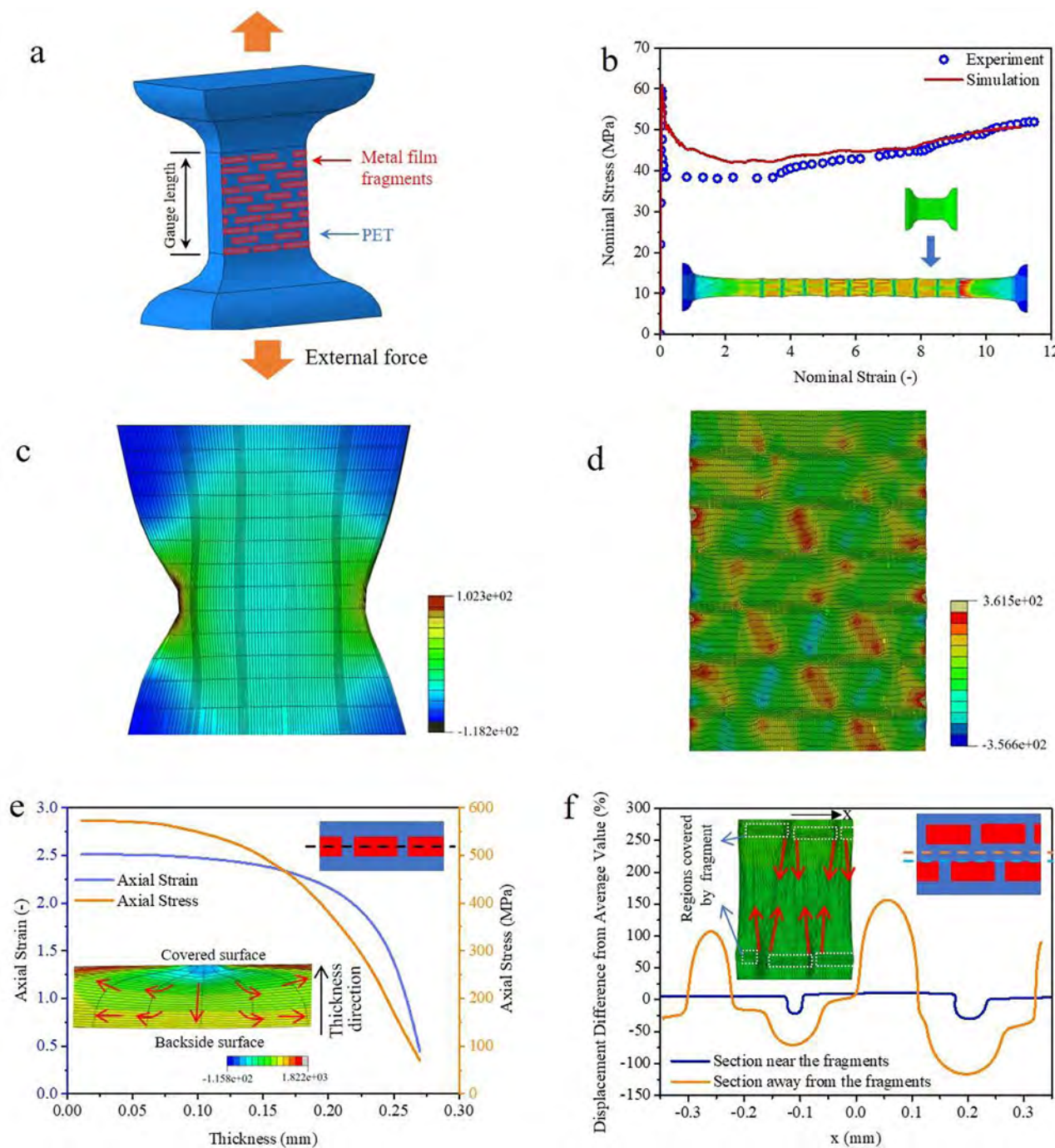


Fig. 4. FEM model of the MZC/PET composite. (a) Schematic diagram of the model; (b) stress-strain curves of the calculated PET and MZC/PET models and their distributions; (c) curves of the axial strain and stress varying with the thickness, with the chosen path and flow schematic of the molecular chains in the thickness direction displayed in the inset; (d) curves of the isolines of the axial displacements on the paths adjusted to and away from the fragments, with the flow schematic of the molecular chains in the plane listed inset; (e, f) stress localization in the PET and MZC/PET sample before breaking.

with some overlap caused by the turning. This fracture process repeated cyclically throughout the deformation process and eventually formed the final sample shape under large strains (Fig. 3(d)). During the deformation, the metal fragments combined with the covered polymers to form stiff regions, while the exposed polymers connecting these stiff regions acted as soft regions. This self-assembled combination of stiff and soft regions constitutes the laminated structure of the nacre, as shown in Fig. 3(e) [38]. Although the size and proportions of the fragments are not equivalent to those of real nacre and nacre-like materials, the deformation mechanism is the same, which will be discussed below.

To further understand the mechanism of the tensile behaviour of MZC/PET composites, an FEM model was built to reveal the details of the deformation, as shown in Fig. 4(a). Before the stress reaches the maximum point, the model predicts the deformation very well (Fig. 4(b)). The shock and instability in the simulation cause the calculated stress reduction to be a little smoother than the experimental data after the stress overshoot, combined with a slight oscillation caused by the algorithm, which does not affect the validity of the model.

The distributions of the stress in the PET and MZC/PET before breakage are shown in Fig. 4(c) and (d), respectively. Under

tension, PET clearly exhibits a necking region with a significant stress concentration that leads to rupture. In contrast, MZC/PET with the nacre-like metal fragments does not exhibit the expected large necking region but instead splits into many small shear bands (red areas) with different orientations, as shown in Figs. 1 and 4(d). The shear bands initiate in the gaps between the metal fragments and extend at 45° to the tensile direction, and their growth is stopped by the metal fragments before crossing through the whole material, which leads to a more localized deformation of the MZC/PET composite in a small region with several fragments. But the overall deformation is more uniformly distributed over the entire specimen compared to the case in PET, which contributes to the toughening of the material. This is similar to another mechanism of reinforcing and toughening of nacre, where cracks are blocked by the organic layers separating the aragonite platelets, allowing the material to continue deforming without failure [46]. In short, two main strengthening and toughening mechanisms derived from nacre structure are integrated in MZC/PET composites, namely cracks blocking with metal fragments and the relative sliding of stiff and soft regions.

3.5. Nonaffine flow of the network

As illustrated in Fig. 1, during the stretching process, the molecular chains of the PET are oriented with the help of the MZC. This molecular chain orientation is confirmed preliminarily by the different fracture surface morphologies of the PET and MZC/PET, as shown in Fig. S7. The fracture surfaces of the PET are perpendicular to the load direction, which implies that there is tension-controlled necking and breaking (Fig. S7(a)). A few of the samples with the fracture surfaces show a combination of a series of fracture segments at 45° to the load direction, referring to a shear-controlled fracture. Both these two fracture patterns are consistent with the strength theory of material mechanics. In contrast, for the MZC/PET composite, the fracture surface shows numerous large cracks along the load direction (Fig. S7(b)), designated 'sideways cracks' by Lee et al. [47]. According to the continuum theory of fracture mechanics, in a tension test, this is the most difficult direction for cracks to evolve in. The presence of this kind of cracks therefore indicates that the fracture energy (or the fracture toughness) required to extend along the load direction is much lower than that perpendicular to it. In highly oriented PET, the van der Waals forces and hydrogen bonds between the molecular chains are much weaker than the covalent bonds within them, resulting in the occurrence of sideways cracks [47]. Therefore, the appearance of sideways cracks indicates the highly oriented form of the molecular chains in the MZC/PET composite.

To investigate the molecular chain orientation in the MZC/PET composite, further characterizations were conducted via two-dimensional wide-angle X-ray diffraction (2D-WAXD) techniques. The 2D-WAXD patterns of PET and MZC/PET composites at different stretching stages are shown in Fig. 5(a–h). The amorphous rings were observed in the unstretched PET and MZC/PET composites, indicating the molecular chains were randomly and disorderly entanglement. When the strain increased to 30%, there were two diffraction arcs in the axial direction, which were symmetrically distributed along the central axis in both the PET and MZC/PET composite 2D-WAXD patterns. When PET was stretched uniaxially, the long molecular chains in the polymer were stretched and aligned along the stretching direction, where molecular orientation and strain-induced crystallisation occurs. Fig. 5(i) and (j) show the azimuthal scan curves of the (100) plane of PET and MZC/PET composites, respectively, which also demonstrate this orientation. With the strain increased to 70%, the polymer molecule chains aligned in the tensile direction and formed small ordered regions, and some weak crystalline ring reflections could be observed. When

the strain reached 150%, the intensity of the patterns of both PET and MZC/PET became stronger, while the one of MZC/PET composites was much stronger than that of PET, which indicates the higher orientation of the molecular chains inside the polymer. This high oriented state of the polymer in the composite makes the chains distribute more parallel with each other, reducing the energy barrier for crystallizing, thus results in a high crystallinity. At the same strain, the more oriented state of the polymer has a stronger bearing capability due to the higher fracture energy of the covalent bonds compared to the van der Waals forces, which allows a continuous deformation at the break strain of the polymer without coating, achieving the toughening effect. These corroborating observations should make an important contribution to understanding the novel mechanisms that contribute to polymer toughening.

There are three diffraction rings in the equatorial direction: specifically, the (010), (1₋₁₀) and (100) crystal planes [48]. As the deformation increased, the diffraction rings in the equatorial direction became sharper and stronger, indicating that the degree of crystallinity had increased. The equatorial radial integrations of the 2D-WAXD patterns of PET and MZC/PET composites are shown in Fig. 5(k) and (l), respectively. The characteristic peaks of the stretched PET and MZC/PET composite films under different tensile strains (30%, 70%, 100%, 150%, 230%) are observed at $2\theta = 17.2^\circ$, 22.6° and 26.8° , which are assigned to the (010), (1₋₁₀) and (100) planes, respectively. This further confirms that the PET began to crystallise after experiencing the tensile process. As the strain increased from 30% to 230%, the intensity of all of the peaks increased. More importantly, the diffraction peak intensities of the stretched MZC/PET composites exceeded those of the PET. This indicates that the MZC amorphous coating promoted the orientation of the polymer molecules, and thus their crystallisation during the stretching process. This increased crystallinity thereby improved the tensile strength and toughness of the composite material.

The deformation gradient of the composite during tension was simulated through FEM presented in Fig. 4(e) and (f) for two typical cases. A path under the fragments is extracted along the thickness direction (shown in the inset of Fig. 4(e)), with the axial stress and strain along it shown in Fig. 4(e). The gradient of both the stress and strain is huge that the value of stress and strain decreases by more than 80% from the backside to the covered side. In metallic or other homogeneous materials, such large stress and strain fluctuations can lead to significant stress concentration and earlier fracture. However, the flow mechanism in polymers makes the situation more complex. In the tensile of the PET, the deformation was uniform, in which affine deformation of the molecular chain network dominant. The molecular chains oriented in affine deformation, and the strength of the material were the consequence of the combined energy required to break the covalent bonds and overcome the van der Waals forces. In the MZC/PET composite, the large deformation gradient induced by the metal fragments leads to nonaffine deformation within the PET matrix, with the entanglement points flowing or diffusing to cause an additional displacement along the gradient direction besides the affine contribution. In the thickness direction, the entanglement points of the network flowed from the small-strain region to the large one, maximising the entropy decrease and homogenising the free volume, as shown in Figs. 1 and 4(e). Besides the flow in the thickness direction, the strain distribution on the covered surface was also inhomogeneous. After the composite material is stretched, the metal film deposited forms nacre-like fragments, and the strength and size of the fragments (the size of the fragments caused by the surface morphology of the interface between the film and the polymer material) have a certain confinement effect on the polymer. The strength of the fragments determines the magnitude of the strain gradient, and the size and

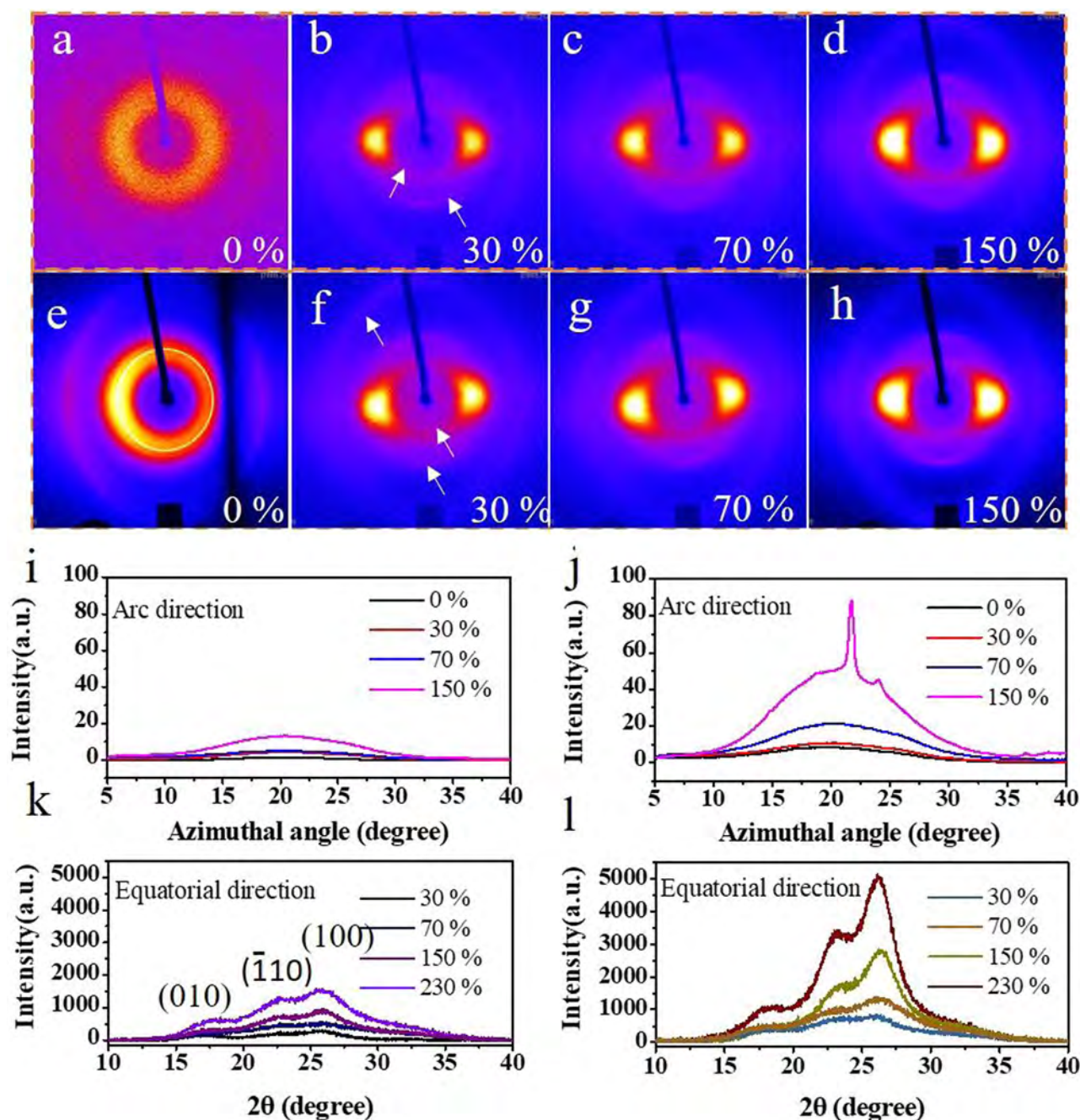


Fig. 5. 2D-WAXD patterns of PET and MZC/PET composites: (a–h) 2D-WAXD diffraction patterns; (i, j) meridian integral diffraction intensities; (k, l) integral diffraction intensity along the equatorial line.

distribution of the fragments (geometric factors such as spacing) determine the distribution of the strain gradient, which together lead to the orientation behavior of the molecular chain. The strain gradient within the polymer only occurs when there is a strain difference between the two sides of the PET film. Therefore, after coating both sides of PET, we consider the limiting case where the strain gradient difference between the two sides is very small when the front and back metal fragments are aligned in parallel, as demonstrated in Fig. S8, so that the molecular chain orientation effect and the toughening effect become very weak. That's the reason why the mechanical performance of the double-sided composites is lower than those of the single-sided coated films. The displacement contours of the path passed through the covered surface at two different locations (crossing and away from the metal

fragments) are presented in Fig. 4(f). Due to the confinement of the metal fragments, the axial displacement near the metal was almost uniform, while the transverse (direction perpendicular to the stretching direction of the covered surface) deformation was borne by the small regions confined by the fragments, as shown in the inset of Fig. 4(f). This heterogeneous transverse deformation caused material to flow away from the confined region to match the deformation compatible conditions, leading to a maximum deviation of 150%, which results in a magnified nonuniform deformation, as shown in Fig. 4(f). The nonaffine deformations of the coated PET in thickness and transverse direction made its orientation degree larger than that of the uncoated PET at the same strain, which is also verified by the 2D-WAXD measurements described above.

4. Conclusions

Combining an amorphous alloy with PET resulted in a composite with an elongation at break of 1180% and a very high toughness of 506.9 MJ/m³. This enhancement is attributed to a new toughening mechanism. The deformation process of the MZC/PET composite after uniaxial stretching is similar to that of nacre, and the amorphous alloy coating is broken into regular fragments similar to the rigid region of nacre-like materials. The relative rotation and sliding of the fragments during deformation dissipate additional energy and prevent the evolution of shear bands. And the rigid region formed by the fragments forces the molecular chains in the confined region to flow to the non-confined region in the plane, forming a nonaffine flow. Both of these cause the orientation of molecular chains and the crystallization of specific crystal phases, resulting in strengthening and toughening. This is a novel mechanism for toughening polymer material that the more homogeneous stress and strain field without concentration, the stronger and tougher the material is. The newly reported toughening mechanism surely could be applied on other composites with polymer component. According to current study, the conditions of wide application of the toughening mechanism could be summarized as: (i) The polymer has the ability to achieve the orientation under sufficient thermodynamic conditions. (ii) The combination of metal and polymer should also be strong enough to limit the strain of the interface of the polymer. (iii) The metal film material is preferably brittle, the strength of the metal material itself is strong enough, which determines the magnitude of the strain gradient. In addition, the choice of the thickness of the polymeric base material and the geometric parameters of the fracture fragments are essential for the toughening effect of the composite. These superior toughness composites with new mechanism may play an increasingly central role in emerging applications, such as improving the biomechanical compatibility of electronic devices and finding promising applications in armour engineering and aerospace engineering. This will open a creative route to designing robust polymeric materials for a range of innovative future applications.

Acknowledgments

This work was financially supported by the Shenzhen-Hong Kong Science and Technology Innovation Cooperation Zone Shenzhen Park Project (No. HZQB-KCZYB-2020030), the RGC General Research Fund (No. AoE/M-402/20, CityU 11209918), the RGC Theme-based Research Scheme (No. T13-402/17-N), and the Major Program of Changsha Science and Technology Project (No. kh2003023).

Supplementary materials

Supplementary material associated with this article can be found, in the online version, at doi:10.1016/j.jmst.2022.05.063.

References

- [1] J.W. Hong, Y. Kim, D.H. Wi, S. Lee, S.U. Lee, Y.W. Lee, S. Il Choi, S.W. Han, *Angew. Chem. Int. Ed.* 55 (2016) 2753–2758.
- [2] V. Chawla, M. Ruoho, M. Weber, A. Chaaya, A. Taylor, C. Charmette, P. Miele, M. Bechelany, J. Michler, I. Utke, *Nanomaterials* 9 (2019) 88.
- [3] P. Cordier, F. Tournilhac, C. Soulié-Ziakovic, L. Leibler, *Nature* 451 (2008) 977–980.
- [4] D. Seliktar, *Science* 336 (2012) 1124–1128.
- [5] A. Amini, A. Khavari, F. Barthelat, A.J. Ehrlicher, *Science* 373 (2021) 1229–1234.
- [6] L. Chen, H.B. Zhao, Y.P. Ni, T. Fu, W.S. Wu, X.L. Wang, Y.Z. Wang, *J. Mater. Chem. A* 7 (2019) 17037–17045.
- [7] Y.J. Yoo, J.H. Lim, G.J. Lee, K.I. Jang, Y.M. Song, *Nanoscale* 9 (2017) 2986–2991.
- [8] Y. Zhang, Y. Li, W. Liu, *Adv. Funct. Mater.* 25 (2015) 471–480.
- [9] M.K. Shin, B. Lee, S.H. Kim, J.A. Lee, G.M. Spinks, S. Gambhir, G.G. Wallace, M.E. Kozlov, R.H. Baughman, S.J. Kim, *Nat. Commun.* 3 (2012) 650.
- [10] S. Paszkiewicz, I. Irska, E. Piesowicz, *Materials* 13 (2020) 2673.
- [11] W. Li, G. Wang, Z. Jiang, C. Liu, P. Huo, S. Zhang, *J. Appl. Polym. Sci.* 131 (2014) 1–6.
- [12] D. Liu, W.C. Nie, Z.B. Wen, C.J. Fan, W.X. Xiao, B. Li, X.J. Lin, K.K. Yang, Y.Z. Wang, *ACS Macro Lett.* 7 (2018) 705–710.
- [13] N. Kazem, M.D. Bartlett, C. Majidi, *Adv. Mater.* 30 (2018) 1–7.
- [14] L. Du, Z.Y. Xu, C.J. Fan, G. Xiang, K.K. Yang, Y.Z. Wang, *Macromolecules* 51 (2018) 705–715.
- [15] M. Borghetti, M. Serpelloni, E. Sardini, S. Pandini, *Sens. Actuat. A Phys.* 243 (2016) 71–80.
- [16] K. Liu, L. Chen, Y. Chen, J. Wu, W. Zhang, F. Chen, Q. Fu, *J. Mater. Chem.* 21 (2011) 8612–8617.
- [17] D. Kaneko, T. Tada, T. Kurokawa, J.P. Gong, Y. Osada, *Adv. Mater.* 17 (2005) 535–538.
- [18] K. Sheng, S. Zhang, S. Qian, C.A. Fontanillo Lopez, *Compos. Part B-Eng.* 165 (2019) 174–182.
- [19] M.T.I. Mredha, Y.Z. Guo, T. Nonoyama, T. Nakajima, T. Kurokawa, J.P. Gong, *Adv. Mater.* 30 (2018) 1–8.
- [20] K. Kobayashi, Y. Ura, S. Kimura, J. Sugiyama, *Adv. Mater.* 30 (2018) 1–6.
- [21] S. Seyedin, J.M. Razal, P.C. Innis, R. Jalili, G.G. Wallace, *Adv. Mater. Interfaces* 3 (2016) 1–10.
- [22] S. Qian, K. Sheng, *Compos. Sci. Technol.* 148 (2017) 59–69.
- [23] D. Blond, V. Barron, M. Ruether, K.P. Ryan, V. Nicolosi, W.J. Blau, J.N. Coleman, *Adv. Funct. Mater.* 16 (2006) 1608–1614.
- [24] J. Li, Y. Durandet, X. Huang, G. Sun, D. Ruan, *J. Mater. Sci. Technol.* 119 (2022) 219–244.
- [25] N. Lu, Z. Suo, J.J. Vlassak, *Acta Mater.* 58 (2010) 1679–1687.
- [26] N. Lu, X. Wang, Z. Suo, J. Vlassak, *Appl. Phys. Lett.* 91 (2007) 221909.
- [27] Y. Xiang, T. Li, Z. Suo, J.J. Vlassak, *Appl. Phys. Lett.* 87 (2005) 161910.
- [28] S.P. Lacour, D. Chan, S. Wagner, T. Li, Z. Suo, *Appl. Phys. Lett.* 88 (2006) 204103.
- [29] Z. Ma, J. Li, J. Zhang, A. He, Y. Dong, G. Tan, M. Ning, Q. Man, X. Liu, *J. Mater. Sci. Technol.* 81 (2021) 43–50.
- [30] S. Gupta, M. Dixit, M. Baboo, K. Sharma, N.S. Saxena, *Polym. Plast. Technol. Eng.* 48 (2009) 1333–1337.
- [31] S. Wang, *Nonlinear Polymer Rheology*, Wiley, Hoboken, 2017.
- [32] E. Goulet, J.M. Haudin, N. Billon, *Polymer* 42 (2001) 9541–9549.
- [33] A. Larranaga, E. Lizundia, *Strain-Induced Crystallization*, Elsevier, Amsterdam, 2018.
- [34] R.B. Dupaux, M.C. Boyce, *Polymer* 46 (2005) 4827–4838.
- [35] T. Magrini, F. Bouville, A. Lauria, H.L. Ferrand, T.P. Niebel, A.R. Studart, *Nat. Commun.* 10 (2019) 2794.
- [36] A. Wat, J.I. Lee, C.W. Ryu, B. Gludovatz, J. Kim, A.P. Tomsia, T. Ishikawa, J. Schmitz, A. Meyer, M. Alfreider, D. Kiener, E.S. Park, R.O. Ritchie, *Nat. Commun.* 10 (2019) 961.
- [37] Z. Mao, M. Huo, F. Lyu, Y. Zhou, Y. Bu, L. Wan, L. Pan, J. Pan, H. Liu, J. Lu, *J. Mater. Sci. Technol.* 114 (2022) 172–179.
- [38] H.D. Espinosa, J.E. Rim, F. Barthelat, M.J. Buehler, *Prog. Mater. Sci.* 54 (2009) 1059–1100.
- [39] S. Askarinejad, N. Rahbar, *Int. J. Plast.* 107 (2018) 122–149.
- [40] G. Du, A. Mao, J. Yu, J. Hou, N. Zhao, J. Han, Q. Zhao, W. Gao, T. Xie, H. Bai, *Nat. Commun.* 10 (2019) 800.
- [41] L. Xia, Q. Zhang, X. Zhuang, S. Zhang, C. Duan, X. Wang, B. Cheng, *Polymers* 11 (2019) 1547.
- [42] J. Berger, M. Reist, J.M. Mayer, O. Felt, N.A. Peppas, R. Gurny, *Eur. J. Pharm. Biopharm.* 57 (2004) 19–34.
- [43] P. Song, Z. Xu, M.S. Dargusch, Z. Chen, H. Wang, Q. Guo, *Adv. Mater.* 29 (2017) 1704661.
- [44] B. Wang, Z. Li, C. Wang, S. Signetti, B.V. Cunning, X. Wu, Y. Huang, Y. Jiang, H. Shi, S. Ryu, N.M. Pugno, R.S. Ruoff, *Adv. Mater.* 30 (2018) 1–10.
- [45] Y. Leterrier, J. Andersons, Y. Pitton, J.A.E. Manson, *J. Polym. Sci. Part B-Polym. Phys.* 35 (1997) 1463–1472.
- [46] F. Bouville, E. Maire, S. Meille, B. Van De Moortèle, A.J. Stevenson, S. Deville, *Nat. Mater.* 13 (2014) 508–514.
- [47] S. Lee, M. Pharr, *Proc. Natl. Acad. Sci.* 116 (2019) 201820424.
- [48] S. Agrawal, N. Ingle, U. Maity, R.V. Jasra, P. Munshi, *ACS Omega* 3 (2018) 6692–6702.
- [49] J. Zhang, Y. Cui, X. Zuo, J. Wan, Y. Rong, N. Chen, J. Lu, *Sci. Bull.* 66 (2021) 1058–1062.